

ISAR Imaging of a Ship Target Based on Parameter Estimation of Multicomponent Quadratic Frequency-Modulated Signals

Xia Bai, Ran Tao, *Senior Member, IEEE*, Zhijiao Wang, and Yue Wang

Abstract—High-resolution inverse synthetic aperture radar (ISAR) imaging of a ship target is a challenging task because of fluctuation with the ocean waves. The images obtained with a standard range-Doppler algorithm are usually blurred. Consequently, the range-instantaneous-Doppler (RID) technique should be used to improve the image quality. In this paper, the received signal in a range cell is modeled as a multicomponent quadratic frequency-modulated (QFM) signal after range compression and motion compensation, and then a new RID ISAR imaging algorithm is proposed that introduces a new method for estimating parameters of the QFM signal. By defining a new function and using the scaled Fourier transform (SCFT) with respect to the time axis, the coherent integration of auto-terms can be realized via the subsequent Fourier transformation with respect to the lag-time axis, and a peak can be obtained in the 2-D frequency plane, which is appropriate for parameter estimation of the QFM signal to reconstruct RID images. The proposed algorithm is accurate and fast since the defined function has moderate order nonlinearity and the SCFT can be performed via chirp z -transform. Experiments demonstrate the performance of the new algorithm. Comparisons with existing algorithms are also given, which show that the proposed algorithm can efficiently produce a focused image with less fake scatterers.

Index Terms—Inverse synthetic aperture radar (ISAR), quadratic frequency-modulated (QFM) signal, parameter estimation, range-instantaneous-Doppler (RID).

I. INTRODUCTION

INVERSE synthetic aperture radar (ISAR) is a useful all-weather high-resolution radar imaging system for moving targets in the air or on the sea. In ISAR imaging, fine range resolution is attained by transmitting a wideband signal, while its azimuth resolution depends on the relative rotation between the radar and the target [1], [2]. ISAR imaging of a ship target on the sea has attracted much attention of many radar researchers in the past years [3]–[10].

A ship target usually fluctuates with oceanic waves, and its rotational motion (roll, pitch, and yaw) may generate aspect

angle change, which causes high-order Doppler frequency shift. In this case, the classical range-Doppler (RD) algorithm [2] fails in generating a well-focused image. An efficient method to solve this problem is the range-instantaneous-Doppler (RID) imaging technique, in which the scatterers of the target in each range cell are imaged at the locations associated with their instantaneous Doppler frequencies.

There exist two categories of RID techniques: parametric and nonparametric. In nonparametric RID techniques [11]–[13], the Fourier transform in the RD algorithm that is used in the azimuth focusing is replaced by the time–frequency representation (TFR), such as short-time Fourier transform (STFT) and Wigner–Ville distribution (WVD). However, these TFRs have some problems for ISAR application. The STFT usually has lower resolution, which is inherently limited by the uncertainty principle. Because of the bilinear nature, high-resolution WVD generally suffers from the cross-term interference. To suppress the cross-term interference, the SPWVD-based method [3], [9], [14] and the LCPWVD-based method [8] were presented, but at the cost of resolution loss.

Parametric RID techniques could avoid geometric resolution loss. Generally, these methods model the received signal as a multicomponent polynomial phase signal (PPS), and estimate parameters of each component to reconstruct focused RID images. In [4], [15], and [16], the assumption is made that, during the imaging time, the received signal can be modeled as a multicomponent linear frequency modulated (LFM) signal. However, when high-order phase terms exist, these methods will suffer performance degradation. Then the received signal is modeled as a multicomponent quadratic frequency-modulated (QFM) signal (also known as cubic phase signal) in [5], [7], and [17]. In [5], an ISAR imaging algorithm is presented which is based on TC-DechirpClean, but this algorithm suffers from heavy computational burden. In [7], the authors proposed the product high-order matched phase transform (PHMT) for ISAR imaging. Because of the high order of nonlinearity (sixth-order to be exact), too many artifacts will present in the image obtained by using the PHMT algorithm. Recently, the ISAR imaging algorithm based on the product generalized cubic phase function (PGCPF) with only fourth-order nonlinearity was proposed in [17]. But the PGCPF technique has high computational complexity.

This paper is aimed at proposing an efficient and accurate parameter estimation method of multicomponent QFM signal for ISAR imaging. The proposed method is based on a newly

Manuscript received July 27, 2012; revised January 5, 2013; accepted February 15, 2013. Date of publication May 7, 2013; date of current version December 12, 2013. This work was supported in part by the National Key Basic Research Program Founded by the Ministry of Science and Technology under Grant 2009CB724003 and Grant 2010CB731902, the National Natural Science Foundation of China under Grant 60890072 and Grant 60119944, and the Program for Changjiang Scholars and Innovative Research Team in University under Grant IRT1005.

The authors are with the Department of Electronic Engineering, Beijing Institute of Technology, Beijing 100081, China (e-mail: bai@bit.edu.cn; rantao@bit.edu.cn; shouji.wang@163.com; wangyue@bit.edu.cn).

Color versions of one or more of the figures in this paper are available online at <http://ieeexplore.ieee.org>.

Digital Object Identifier 10.1109/TGRS.2013.2251348

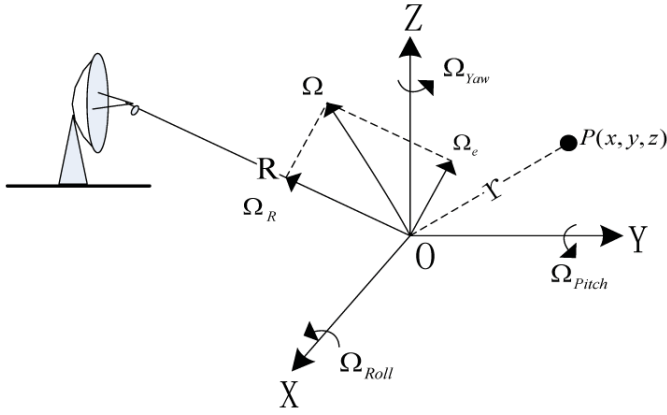


Fig. 1. ISAR imaging geometry.

defined function with fourth-order nonlinearity and a scaled Fourier transform (SCFT) with respect to the time axis. The SCFT can transform the original curved distributed signal spectrum line into a beeline parallel to the lag-time axis. Then coherent integration of auto-terms based on a Fourier transform with respect to the lag-time axis can effectively suppress the cross-term interference. Compared with the methods based on PHMT and PGCPF, the proposed estimator is accurate, and does not suffer from heavy computational burden by using the chirp- z transform (CZT). It is more suitable to be combined with RID technique for the high-quality ISAR imaging of a ship target.

The remainder of this paper is organized as follows. In Section II, the multicomponent QFM signal model for the received signal is established. In Section III, a new parameter estimation method is presented in detail. Its application to ISAR imaging for a ship target is illustrated in Section IV. The experiments with simulated data and real data are made to verify the effectiveness of the novel algorithm in Section V. Finally, Section VI gives the conclusion.

II. SIGNAL MODEL

The geometry for ISAR imaging used here is based on the model described in [7]. We assume that the ship target rotation outside the plane between the radar and target is small, and standard range alignment has been applied to the data so that the coarse translational motion has been removed. All the scatterers stay in the right range cells.

The ISAR imaging geometry is shown in Fig. 1. The ship target is described in the Cartesian coordinates with the origin located at the rotation center, called body coordinates of the target. The unit vector of the radar line of sight (LOS) is \mathbf{R} . The X , Y , and Z axes overlap with the longitudinal, horizontal, and vertical axes of the target, respectively. Vectors Ω_{Roll} , Ω_{Pitch} , and Ω_{Yaw} represent the angular rotation vectors of the target rotating around the X , Y , and Z axes. Let Ω denotes the synthetic vector of Ω_{Roll} , Ω_{Pitch} , and Ω_{Yaw} . It can be decomposed into two components Ω_R and Ω_e in the plane determined by Ω and \mathbf{R} , where Ω_R is the component parallel to \mathbf{R} , and Ω_e is the component perpendicular to \mathbf{R} . Ω_R does not cause radial motion and thus has no effect on the phase

of the echo signal. Ω_e , which is called the effective rotation vector, gives rise to the Doppler frequency shift.

The position of a scatterer \mathbf{P} on the target is denoted by the vector $\mathbf{r}(x, y, z)$. Its Doppler frequency has the following form:

$$f_d = \frac{2(\Omega_e \times \mathbf{r}) \cdot \mathbf{R}}{\lambda} \quad (1)$$

where “ \times ” and “ \cdot ” represent the outer and inner products, respectively, and λ denotes the wavelength. The effective rotation vector of a ship target on the sea is usually time-varying, and Ω_e can be approximated as

$$\Omega_e(t) = \alpha + \omega t + \frac{1}{2}\gamma t^2 \quad (2)$$

where α is the constant term, ω and γ are coefficients of the first-order and second-order terms of $\Omega_e(t)$, respectively, and t is the azimuth time (or slow time). Note that (2) also holds for short observation time. In practice, the ISAR imaging time is usually very short. By substituting (2) into (1), we have

$$f_d(t) = \frac{2}{\lambda} \left\{ (\alpha \times \mathbf{r}) \cdot \mathbf{R} + [(\omega \times \mathbf{r}) \cdot \mathbf{R}]t + \left[\frac{1}{2}(\gamma \times \mathbf{r}) \cdot \mathbf{R} \right]t^2 \right\}. \quad (3)$$

From (3), it can be noted that the distance from scatterer \mathbf{P} to radar can be expressed as

$$\begin{aligned} R(t) &= \int_{t_0}^t -\frac{\lambda}{2} f_d(t) dt \\ &= \int_{t_0}^t - \left\{ (\alpha \times \mathbf{r}) \cdot \mathbf{R} + [(\omega \times \mathbf{r}) \cdot \mathbf{R}]t + \left[\frac{1}{2}(\gamma \times \mathbf{r}) \cdot \mathbf{R} \right]t^2 \right\} dt \\ &= R_0 - [(\alpha \times \mathbf{r}) \cdot \mathbf{R}]t - \frac{1}{2}[(\gamma \times \mathbf{r}) \cdot \mathbf{R}]t^2 \\ &\quad - \frac{1}{6}[(\gamma \times \mathbf{r}) \cdot \mathbf{R}]t^3 \end{aligned} \quad (4)$$

where t_0 denotes the initial time of ISAR imaging, R_0 denotes the corresponding initial distance from radar to the target center and the scope of t is $[-T/2, T/2]$, where T denotes the azimuth imaging time. Hence, after range compression and motion compensation, the azimuth signal of the scatterer \mathbf{P} has the following QFM form:

$$s_p(t) = \sigma_p \exp \left[-j \frac{4\pi}{\lambda} R(t) \right]. \quad (5)$$

So it is obvious that the received signal from all scatterers in one range cell can be modeled as a multicomponent QFM signal [5], [7], [17] after range compression and motion compensation

$$s(t) = \sum_{i=1}^K \sigma_i \exp \left(j2\pi a_{i,1}t + j2\pi a_{i,2}t^2 + j2\pi a_{i,3}t^3 \right) \quad (6)$$

where σ_i is the amplitude of the i th component; $a_{i,1}$, $a_{i,2}$, and $a_{i,3}$ are the phase coefficients; and K is the number of the components. Note that the constant phase term is omitted in (6), because it does not affect the imaging result.

III. METHOD FOR PARAMETER ESTIMATION

A. Principle

Consider a QFM signal

$$x(t) = \exp(j2\pi a_1 t + j2\pi a_2 t^2 + j2\pi a_3 t^3). \quad (7)$$

We construct a new function

$$y(t, \tau) = x(t + \tau) x(t - \tau) x^*(t) x^*(t) \quad (8)$$

where τ is the lag time, and $*$ denotes complex conjugate. Substituting (7) into (8) yields

$$y(t, \tau) = \exp(j4\pi a_2 \tau^2 + j12\pi a_3 \tau^2 t). \quad (9)$$

By taking an SCFT of $y(t, \tau)$ with respect to t , we have

$$\begin{aligned} Y_1(f_t, \tau) &= \int y(t, \tau) \cdot \exp(-j2\pi f_t \beta t) d(\beta t) \\ &= \int \exp\left[-j2\pi \left(f_t - \frac{6a_3 \tau^2}{\beta}\right) \beta t\right] d(\beta t) \\ &\quad \cdot \exp(j4\pi a_2 \tau^2) \\ &= \delta\left(f_t - \frac{6a_3 \tau^2}{\beta}\right) \exp(j4\pi a_2 \tau^2) \end{aligned} \quad (10)$$

where f_t is the frequency corresponding to t , and β is the scale factor. It can be noted that (10) becomes a Fourier transform of $y(t, \tau)$ when $\beta = 1$

$$\begin{aligned} Y_{1FT}(f_t, \tau) &= \int y(t, \tau) \cdot \exp(-j2\pi f_t t) dt \\ &= \delta(f_t - 6a_3 \tau^2) \exp(j4\pi a_2 \tau^2). \end{aligned} \quad (11)$$

From (11), it can be seen that the peaks of $Y_{1FT}(f_t, \tau)$ locate on the curve line $f_t = 6a_3 \tau^2$ in the $f_t - \tau$ plane. If the coupling between the frequency f_t and lag time τ is removed, the coherent integration of the signal can be performed via a Fourier transform with respect to the lag time.

Now we let $\beta = \tau^2$, and then (10) can be rewritten as

$$\begin{aligned} Y_1(f_t, \tau) &= \int y(t, \tau) \cdot \exp(-j2\pi f_t \tau^2 t) d(\tau^2 t) \\ &= \exp(j4\pi a_2 \tau^2) \delta(f_t - 6a_3). \end{aligned} \quad (12)$$

It is obvious from (12) that the peaks of $Y_1(f_t, \tau)$ locate on the line $f_t = 6a_3$ parallel to the τ -axis. Thus the SCFT with $\beta = \tau^2$ can decouple the frequency f_t and the lag time τ , and the signal can be coherently integrated by the transform as

$$Y_2(f_t, f_\tau) = \int Y_1(f_t, \tau) \cdot \exp(-j2\pi f_\tau \tau^2) d\tau^2$$

$$\begin{aligned} &= \delta(f_t - 6a_3) \int \exp[-j2\pi (f_\tau - 2a_2) \tau^2] d\tau^2 \\ &\approx \delta(f_t - 6a_3) \delta(f_\tau - 2a_2) \end{aligned} \quad (13)$$

where f_τ is the frequency corresponding to τ . Hence the parameters a_3 and a_2 can be estimated by searching the peak values of $Y_2(f_t, f_\tau)$ in the $f_t - f_\tau$ plane, respectively

$$(f_{t0}, f_{\tau 0}) = \arg \max_{f_t, f_\tau} |Y_2(f_t, f_\tau)| \quad (14)$$

$$\hat{a}_3 = \frac{1}{6} f_{t0} \quad (15)$$

$$\hat{a}_2 = \frac{1}{2} f_{\tau 0}. \quad (16)$$

Other parameters can be estimated by the dechirp technique and the Fourier transform according to the maximum magnitude criteria after compensating for higher order phase terms [7], [17].

B. Numerical Implementation

We consider the discrete form of the QFM signal given by (7)

$$x(n\Delta t) = \exp[j2\pi a_1 n\Delta t + j2\pi a_2 (n\Delta t)^2 + j2\pi a_3 (n\Delta t)^3] \quad (17)$$

where $n = -N/2, \dots, N/2 - 1$, N is the number of the samples and is assumed to be even, and Δt denotes the sampling interval. Hence, (8) and (9) can be rewritten as (18), shown at the bottom of the page. Then the scaled discrete Fourier transform of $y(n\Delta t, m\Delta t)$ with respect to $n\Delta t$ is (19), shown at the bottom of the next page. Equation (19) can be computed by the CZT which only needs complex multiplications and the fast Fourier transforms (FFTs) [18], [19]. The scale factor β in the SCFT makes some changes to the spectrum of the signal. In order to implement the scale transform properly, we introduce a constant P_t called the zoom factor. Let $\beta = P_t (m\Delta t)^2$; then (19) can be rewritten as

$$\begin{aligned} Y_1(k, m\Delta t) &= \exp[j4\pi a_2 (m\Delta t)^2 \\ &\quad + j\pi \frac{P_t m^2 \Delta t^2}{N} \left(k - \frac{6N\Delta t}{P_t} a_3\right)] \\ &\quad \cdot \text{sinc}\left[j\pi \frac{P_t m^2 \Delta t^2 (N - 2|m|)}{N}\right] \\ &\quad \cdot \left(k - \frac{6N\Delta t}{P_t} a_3\right). \end{aligned} \quad (20)$$

Similarly, another zoom factor denoted as P_τ is introduced to the subsequent transform. After the discrete Fourier transform

$$y(n\Delta t, m\Delta t) = x(n\Delta t + m\Delta t) x(n\Delta t - m\Delta t) x^*(n\Delta t) x^*(n\Delta t) = \exp[j4\pi a_2 (m\Delta t)^2 + j12\pi a_3 (m\Delta t)^2 (n\Delta t)]$$

where $n = n_{m1}, n_{m1} + 1, \dots, n_{m2}, m = m_{n1} + 1, m_{n1} + 2, \dots, m_{n2}$

$$\begin{aligned} \left(n_{m1} = \max \left\{ -\frac{N}{2}, -m - \frac{N}{2}, m - \frac{N}{2} \right\}, \quad n_{m2} = \min \left\{ \frac{N}{2} - 1, -m + \frac{N}{2} - 1, m + \frac{N}{2} - 1 \right\} \right. \\ \left. m_{n1} = \max \left\{ -n - \frac{N}{2} + 1, n - \frac{N}{2}, -\frac{N}{2} + 1 \right\}, \quad m_{n2} = \min \left\{ -n + \frac{N}{2}, n + \frac{N}{2} - 1, \frac{N}{2} - 1 \right\} \right) \end{aligned} \quad (18)$$

of $Y_1(k, m\Delta t)$ with respect to $d\tau^2 = 2\tau d\tau = 2|m|(\Delta t)^2$, we can obtain

$$\begin{aligned} Y_2(k, l) &= \sum_{m=-N/2+1}^{N/2-1} Y_1(k, m\Delta t) \\ &\quad \cdot \exp\left[-j2\pi P_\tau \frac{1}{N\Delta t}(m\Delta t)^2\right] 2|m|(\Delta t)^2 \\ &= C \sum_{m=-N/2+1}^{N/2-1} |m| Y_1(k, m\Delta t) \\ &\quad \cdot \exp\left[-j2\pi P_\tau \frac{1}{N\Delta t}(m\Delta t)^2\right] \end{aligned} \quad (21)$$

where $C = 2(\Delta t)^2$. According to (20), the peak of $Y_1(k, m\Delta t)$ at each $m\Delta t$ locates at $k_0 = (6N\Delta t/P_\tau)a_3$, which implies that all the peaks locate on the line $k = k_0$. Therefore, the peak of $Y_2(k, l)$ should appear in this line. Substituting $k = k_0$ into (21) and noting that $Y_1(k_0, m\Delta t) = \exp[j4\pi a_2(m\Delta t)^2]$, we can obtain

$$\begin{aligned} Y_2(k_0, l) &= C \sum_{m=-N/2+1}^{N/2-1} |m| \\ &\quad \cdot \exp\left[-j2\pi \frac{P_\tau \Delta t}{N} \left(l - \frac{2N\Delta t}{P_\tau} a_2\right) m^2\right]. \end{aligned} \quad (22)$$

It is easy to get from (22) that $Y_2(k_0, l)$ yields a peak at $l_0 = (2N\Delta t/P_\tau)a_2$. Actually, the weight $|m|$ could take other forms and be adjusted accordingly. The location of peak remains at $l_0 = (2N\Delta t/P_\tau)a_2$ no matter what forms the weight takes. Hence we can determine the coordinates of the peak by solving

$$(k_0, l_0) = \arg \max_{k, l} |Y_2(k, l)|. \quad (23)$$

Then third-order and second-order coefficients of the QFM signal could be estimated as

$$\hat{a}_3 = \frac{P_t}{6} \cdot \frac{1}{N\Delta t} \cdot k_0 \quad (24)$$

$$\hat{a}_2 = \frac{P_\tau}{2} \cdot \frac{1}{N\Delta t} \cdot l_0. \quad (25)$$

Note that the selection of the two zoom factors is very important in the implementation of the proposed method. The selection criterion will be subsequently discussed in numerical examples.

TABLE I
PARAMETERS OF THE SIMULATED SIGNAL

Parameter	σ	a_1	a_2	a_3
Value	1	1/16	1/10N	1/10N ²

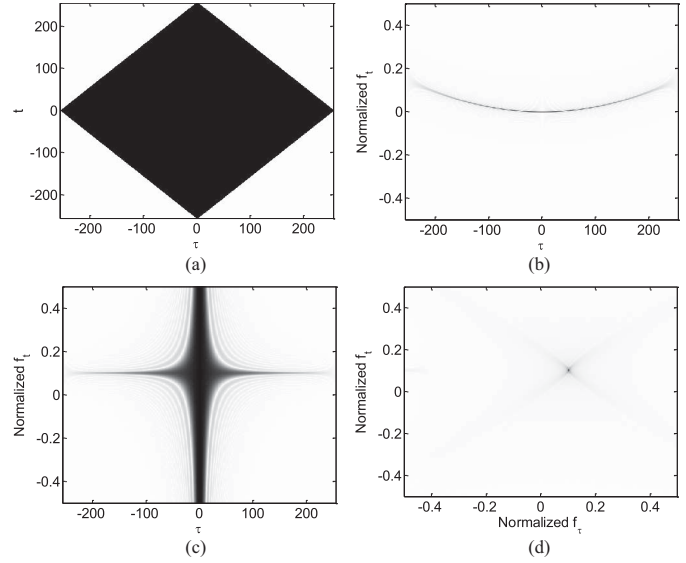


Fig. 2. Results of the monocomponent QFM signal. (a) $y(t, \tau)$. (b) $Y_{1FT}(f_t, \tau)$. (c) $Y_1(f_t, \tau)$. (d) $Y_2(f_t, f_\tau)$.

C. Examples

1) *Processing a Monocomponent QFM Signal:* Consider a monocomponent QFM signal of length N with the following structure:

$$x(n\Delta t) = \sigma \exp\left(j2\pi a_1 n\Delta t + j2\pi a_2 (n\Delta t)^2 + j2\pi a_3 (n\Delta t)^3\right).$$

The sampling rate is assumed to be unity, that is, $\Delta t = 1$. $N = 512$, and $n = -256, -255, \dots, 255$. The parameters are shown in Table I.

Fig. 2(a) plots the amplitude of $y(t, \tau)$ obtained by (8) for the simulated signal. As is shown in Fig. 2(b), the peaks of $Y_{1FT}(f_t, \tau)$ obtained by (11) are located on a curve line, which demonstrates the coupling between f_t and τ . After the scaled transformation shown in (12) for $y(t, \tau)$, the peaks of $Y_1(f_t, \tau)$ locate on a line parallel to the τ -axis

$$\begin{aligned} Y_1(k, m\Delta t) &= \sum_{n=n_{m1}}^{n_{m2}} y(n\Delta t, m\Delta t) \exp\left[-j2\pi \frac{k}{N\Delta t} \beta(n\Delta t)\right] \\ &= \sum_{n=n_{m1}}^{n_{m2}} \exp\left[j4\pi a_2(m\Delta t)^2 + j12\pi a_3(m\Delta t)^2(n\Delta t) - j2\pi \frac{k}{N\Delta t} \beta(n\Delta t)\right] \\ &= \exp\left[j4\pi a_2(m\Delta t)^2 + j\pi \frac{\beta}{N} \left(k - \frac{6Nm^2\Delta t^3}{\beta} a_3\right)\right] \cdot \frac{\sin\left[j\pi \frac{\beta(N-2|m|)}{N} \left(k - \frac{6Nm^2\Delta t^3}{\beta} a_3\right)\right]}{\sin\left[j\pi \frac{\beta}{N} \left(k - \frac{6Nm^2\Delta t^3}{\beta} a_3\right)\right]} \\ &= \exp\left[j4\pi a_2(m\Delta t)^2 + j\pi \frac{\beta}{N} \left(k - \frac{6Nm^2\Delta t^3}{\beta} a_3\right)\right] \cdot \text{sinc}\left[j\pi \frac{\beta(N-2|m|)}{N} \left(k - \frac{6Nm^2\Delta t^3}{\beta} a_3\right)\right] \end{aligned} \quad (19)$$

TABLE II
PARAMETERS ESTIMATION OF THE QFM SIGNAL

Parameter	a_2	a_3
True value	1.9531×10^{-4}	3.8147×10^{-7}
Estimates ($P_t = 3/2N^2$, $P_\tau = 1/2N$)	1.9550×10^{-4}	3.8184×10^{-7}
Estimates ($P_t = 6/N^2$, $P_\tau = 2/N$)	1.9455×10^{-4}	3.7998×10^{-7}
Estimates ($P_t = 24/N^2$, $P_\tau = 8/N$)	1.9836×10^{-4}	3.8743×10^{-7}

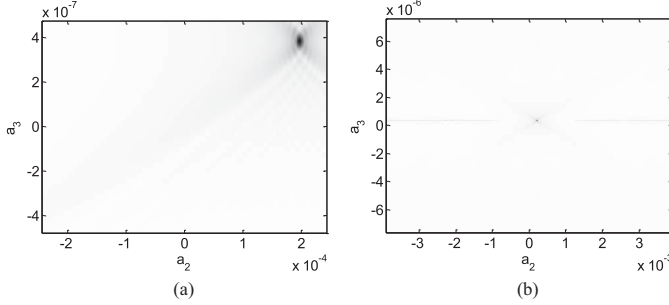


Fig. 3. Results with different values of zoom factors. (a) $P_t = 3/2N^2$, $P_\tau = 1/2N$. (b) $P_t = 24/N^2$, $P_\tau = 8/N$.

[Fig. 2(c)], from which it can be seen that the decoupling has been realized. The width of the beeline line varies with $\tau = m\Delta t$. It shows in (20) that the width of the *sinc* function is $N/[P_t m^2 \Delta t^2 (N - 2|m|)]$, which gives an explanation to this phenomenon. Fig. 2(d) is $Y_2(f_t, f_\tau)$ obtained by (13). It is apparent that $Y_2(f_t, f_\tau)$ yields a peak in the 2-D frequency plane. We can estimate a_3 and a_2 by searching the location of the peak.

Here $P_t = 6/N^2$ and $P_\tau = 2/N$. In order to demonstrate the effect of the zoom factors, the different values listed in Table II are used, and the results are shown in Fig. 3.

From Table II and Fig. 3, it can be seen that a tradeoff between the range and accuracy of the parameter estimation should be considered when selecting P_t and P_τ . Smaller P_t and P_τ generate higher estimation precision but spectrum aliasing might occur. On the contrary, a wider coverage of the frequency spectrum can be obtained by using a larger zoom factor, while less accuracy of estimation or even the spectrum leakage problem can occur because of an overlarge frequency cell. To arrive at a tradeoff, we suggest $P_t = 6/N^2$ and $P_\tau = 2/N$ empirically. For the selection criterion of the two zoom factors, refer to Appendix A.

2) *Processing a Multicomponent QFM Signal*: Consider a multicomponent signal of length N with the structure

$$s(n\Delta t) = \sum_{i=1}^2 \sigma_i \exp \left(j2\pi a_{i,1} n\Delta t + j2\pi a_{i,2} (n\Delta t)^2 + j2\pi a_{i,3} (n\Delta t)^3 \right).$$

The sampling rate is assumed to be unity, i.e., $\Delta t = 1$. $N = 512$, and $n = -256, -255, \dots, 255$. The parameters are shown in Table III, and the results are shown in Fig. 4. We can see that the cross-terms do not appear by using the proposed method, which is appropriate for the parameter estimation of multicomponent QFM signal.

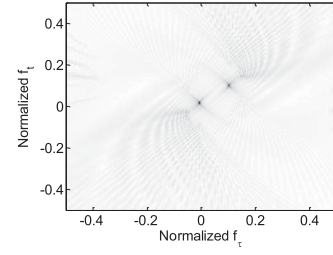


Fig. 4. Results of the multicomponent QFM signal: $Y_2(f_t, f_\tau)$.

TABLE III
PARAMETERS OF THE SIMULATED SIGNAL

Components (i)	σ_i	$a_{i,1}$	$a_{i,2}$	$a_{i,3}$
1	1	1/16	1/10N	1/10N ²
2	1	-1/16	-1/120N	1/60N ²

D. Comparison

Now we compare the proposed method with the methods based on the PHMT [7] and the PGCPF [17] in the aspects of accuracy and efficiency.

The accuracy of a parameter estimation method of multicomponent QFM signal mainly depends on the nonlinearity order and the cross-term suppression. Table IV summarizes the functional considerations of these methods.

PHMT is a high-order nonlinearity transform, which decreases the estimation accuracy. The estimated result by using the PHMT method might contain many artifacts. The PGCPF has the same order of nonlinearity as the proposed method, but it may lead to completely wrong estimation, because the product form sometimes cannot suppress the cross-term (see Appendix B).

The new approach is compared with PHMT and the PGCPF in computational complexity (Table V). The PHMT method with 1-D transform kernel is efficient, while the PGCPF method suffers a heavy computational burden because of the 2-D kernel. Fortunately, the proposed method can be implemented efficiently by using the CZT, though the 2-D transform kernel is also used.

The numerical example is provided to compare the asymptotic statistical performances of PHMT, PGCPF, and the proposed algorithm by the Monte Carlo simulations. The signal embedded in white Gaussian noise is considered. The parameters of the QFM signal are given in Table I. The scope of the input signal-to-noise ratio (SNR) is from -10 to $+10$ dB in steps of 2 dB. Fig. 5(a) and (b) shows the Monte Carlo simulation results using three methods to estimate a_3 and a_2 , respectively, in which 100 trials are used for each SNR. It is seen that these methods provide fairly accurate estimations at high SNRs, and the proposed method has a lower threshold value of SNR than the PHMT and PGCPF methods for the single-component case.

In addition, the method based on PHMT or PGCPF estimates phase coefficients one by one with two 1-D maximizations [Fig. 6(a)]. The new method estimates them simultaneously by searching for the location of the peak in the 2-D

TABLE IV
COMPARISON OF METHODS (1)

Methods	$y(t, \tau)$	The Order of Nonlinearity	The Suppression of Cross-Term
PHMT	$[x^*(t + \tau)x(t - \tau)]^2 [x(t + 2\tau)x^*(t - 2\tau)]$	6	Using product form
PGCPF	$x(t + \tau)x(t - \tau)x^*(-t + \tau)x^*(-t - \tau)$	4	Using product form
NEW	$x(t + \tau)x(t - \tau)x^*(t)x^*(t)$	4	Using scaled transform

TABLE V
COMPARISON OF METHODS (2)

Methods	The Transforms of $y(t, \tau)$	The Dimension of Kernel	Implementation
PHMT	$HMT(t, f_\tau) = \int y(t, \tau) \exp(-j2\pi f_\tau \tau^3) d\tau^3$	1-D (τ)	DFT
PGCPF	$GCPF(t, f_\tau) = \int y(t, \tau) \exp(-j2\pi f_\tau t \tau^2) t d\tau^2$	2-D ($t - \tau$)	DFT
NEW	$Y_1(f_t, \tau) = \int y(t, \tau) \exp(-j2\pi f_t \tau^2 t) \tau^2 dt$	2-D ($\tau - t$)	CZT

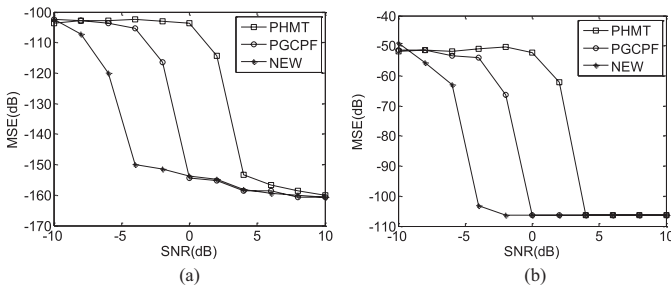


Fig. 5. Performance comparison of the three estimation methods. The MSE (in dB) of (a) a_3 and (b) a_2 versus the SNR, respectively.

plane. It is easy to distinguish adjacent coefficients, so long as the signals differ in another coefficient [Fig. 6(b)].

The above analysis indicates that the proposed parameter estimation method for QFM signals is suitable for the application to ISAR imaging.

IV. ISAR IMAGING

In this section, an ISAR imaging algorithm based on the new parameter estimation method is proposed, in which the clean technique that evaluates each component of the multi-component QFM signal in a descending sequence according to the energy value is employed in the same way as in [7], [17]. The flowchart of the proposed algorithm is illustrated in Fig. 7, and the main steps of the algorithm are listed as follows.

Step 1: Implement range compression and translational motion compensation and initialize $r = 1$.

Step 2: Get r th range cell data and denote the echo signal in the range cell as $s(n\Delta t)$

$$s(n\Delta t) = \sum_{i=1}^K \sigma_i \exp[j2\pi a_{i,1}(n\Delta t)] \cdot \exp[j2\pi a_{i,2}(n\Delta t)^2 + j2\pi a_{i,3}(n\Delta t)^3]$$

where $\Delta t = 1/\text{PRF}$, with PRF denoting the pulse repetition frequency. Initialize $i = 1$, $s_i(n\Delta t) = s(n\Delta t)$.

Step 3.1: Estimate $a_{i,3}$ and $a_{i,2}$ by using the proposed parameter estimation method.

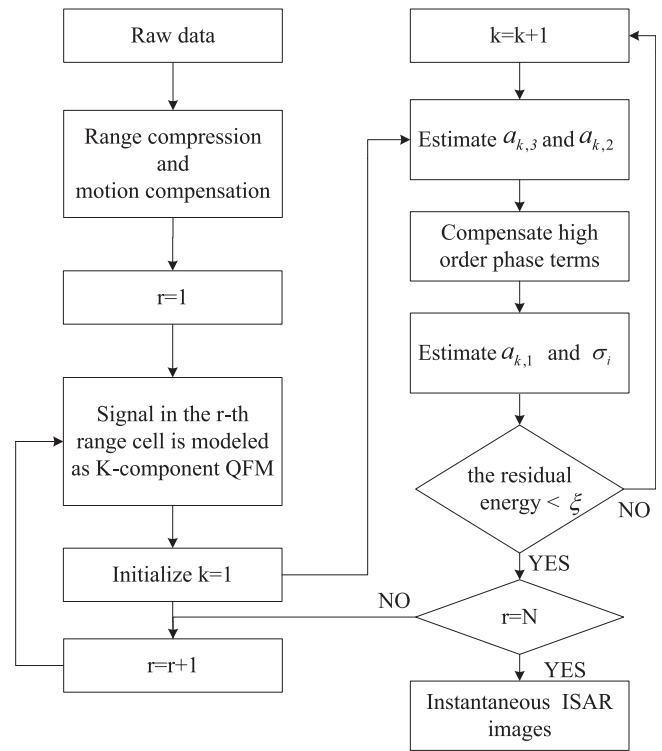


Fig. 7. Flowchart of the proposed ISAR imaging algorithm.

Step 3.2: Construct the reference signal

$$x_{\text{ref}}(n\Delta t) = \exp[-j2\pi \hat{a}_{i,2}(n\Delta t)^2 - j2\pi \hat{a}_{i,3}(n\Delta t)^3]$$

and multiply it with $s_i(n\Delta t)$, obtaining

$$x_d(n\Delta t) = s_i(n\Delta t) \cdot x_{\text{ref}}(n\Delta t).$$

It is obvious that $x_d(n\Delta t)$ becomes a sinusoid.

Step 3.3: Estimate $a_{i,1}$ by searching for the peak of the Fourier transform on $x_d(n\Delta t)$.

Step 3.4: Estimate the amplitude by

$$\sigma_i = \frac{1}{N} \left| \sum_{n=-N/2}^{N/2} s_i(n\Delta t) \cdot \exp[-j2\pi \hat{a}_{i,1}(n\Delta t)] \cdot \exp[-j2\pi \hat{a}_{i,2}(n\Delta t)^2 - j2\pi \hat{a}_{i,3}(n\Delta t)^3] \right|.$$

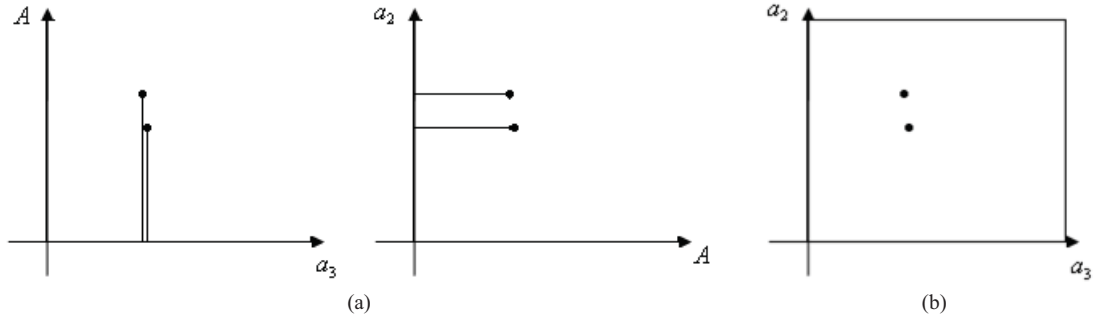


Fig. 6. Estimation of a_3 and a_2 of multicomponent QFM signal with (a) 1-D maximization and (b) 2-D maximization.

Step 3.5: Construct the i th component

$$x_i(n\Delta t) = \sigma_i \cdot \exp[j2\pi\hat{a}_{i,1}(n\Delta t)] \cdot \exp[j2\pi\hat{a}_{i,2}(n\Delta t)^2 + j2\pi\hat{a}_{i,3}(n\Delta t)^3].$$

Subtract it from $s_i(n\Delta t)$ by

$$s_{i+1}(n\Delta t) = \text{IFFT}\{\text{Win}_i(\hat{a}_{i,1}) \cdot \text{FFT}(x_d(n\Delta t))\}$$

where

$$\text{Win}_i(\hat{a}_{i,1}) = \begin{cases} 0, & f_{i,L} < \hat{a}_{i,1} < f_{i,R} \\ 1, & \text{otherwise} \end{cases}$$

is a notch filter centered at the first-order phase coefficient $\hat{a}_{i,1}$.

Step 3.6: Update $i = i + 1$ and repeat steps 3.1–3.6 until $i = K$. In fact, K is unknown in advance. Hence, we can repeat steps 3.1–3.6 until the residual energy of the signal is smaller than a threshold ξ (say 1% of the original signal).

Step 4: Update $r = r + 1$ and return to step 2 until $r = N$. The parameter estimates for all range cells are obtained, and then instantaneous ISAR images at any time can be reconstructed.

V. EXPERIMENTAL RESULTS

In this section, some results with simulated and real data are presented to validate the proposed ISAR imaging algorithm. Comparisons with other algorithms are also given. In order to make a fair comparison, we use the equivalent zoom factors in the three algorithms to ensure the same range of parameter estimation (see Appendix C).

A. Simulated Data

First, a simulation example of a ship target is modeled as a set of ideal scatterers, as presented in Fig. 8(a). The parameters used in the simulation are listed in Table VI. Because the target rotates nonuniformly, the image obtained by the classical RD algorithm is blurred severely [Fig. 8(b)].

For some range cells where the scatterers are located, the component numbers obtained by applying different algorithms are shown in Table VII. We can see that the proposed technique estimates all signals successfully. The reconstructed instantaneous ISAR images via the PHMT-based, the PGCPF-based, and the proposed algorithms are shown in Figs. 9–11, respectively. As expected, the images produced by the PHMT-based algorithm contain many artifacts due to the high order

TABLE VI
PARAMETERS OF THE RADAR SYSTEM

Quantity	Values
Carrier frequency	10 GHz
Bandwidth	150 MHz
Sampling frequency	300 MHz
Pulse repetition frequency	500 Hz
Range of scene center	10 km
Range cells	400
Pulse number	400
Rotating velocity	0.01 rad/s
Rotating acceleration	0.008 rad/s ²
Rotating acceleration rate	0.03 rad/s ³

TABLE VII
COMPONENT NUMBER IN SOME RANGE BINS

	67th Bin	134th Bin	201th Bin	268th Bin	335th Bin
True (K)	3	4	4	2	1
PHMT	5	16	20	2	1
PGCPF	4	4	5	2	1
NEW	3	4	4	2	1

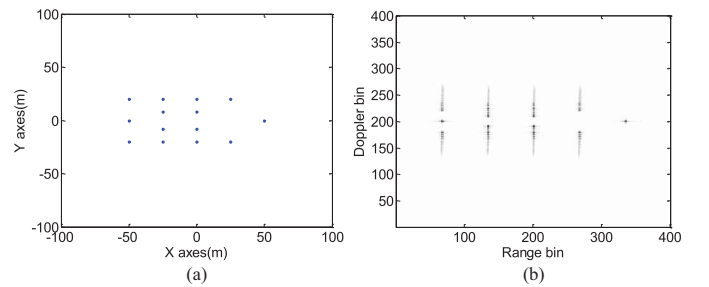


Fig. 8. Simulation. (a) Ship target. (b) Image obtained by using the RD algorithm.

of nonlinearity shown in Table IV. The images obtained by the PGCPF-based and the proposed algorithms have higher quality. In this simulation, the running times of these algorithms are 42, 936, and 84 s, respectively. Apparently, the PGCPF method uses a much longer running time than other two methods, which is due to the usage of the 2-D transform kernel shown in Table V. It is shown that the proposed algorithm has a good performance both in estimation accuracy and computational efficiency in the noiseless case. The advantages

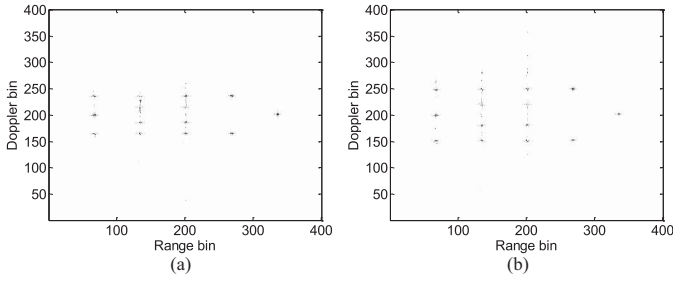


Fig. 9. Images via the PHMT-based algorithm at time (a) $t = 0.198$ s and (b) $t = 0.298$ s.

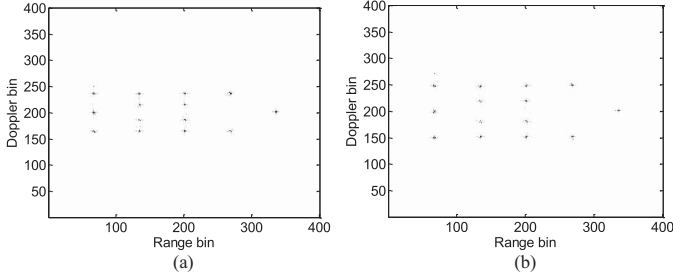


Fig. 10. Images via the PGCPF-based algorithm at time (a) $t = 0.198$ s and (b) $t = 0.298$ s.

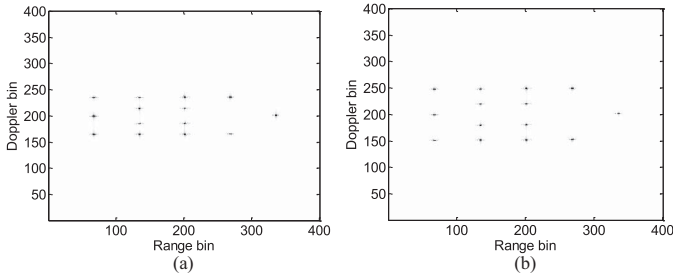


Fig. 11. Images via the proposed algorithm at time (a) $t = 0.198$ s and (b) $t = 0.298$ s.

of the proposed algorithm lie in moderate-order nonlinearity and the efficient CZT.

To better compare the performances of these parameter estimation methods in considered radar application, the range-compressed signals of the range cells listed in Table VII are corrupted by additive white Gaussian noise, and then processed by PHMT, PGCPF, and the proposed method. The reason is that, if noise is added to raw echo of the target, then the SNR level of signal will improve greatly by the range compression and it cannot directly demonstrate the performances of these estimation methods in the case of noise.

Monte Carlo simulation results quantify the variation of estimated component number ($\Delta K = \hat{K} - K$) with respect to the SNR, in which 100 trials are used for each SNR. From the statistical analysis shown in Fig. 12, it is seen that the proposed method and the PGCPF method have similar estimation performances and both of them have better robustness than the PHMT method. Moreover, the component number of the signal denoted by K is also a considerable influencing factor on performance in the noiseless or noisy case. The more the number of components in the signal, the more the number of artifacts in the PHMT method.

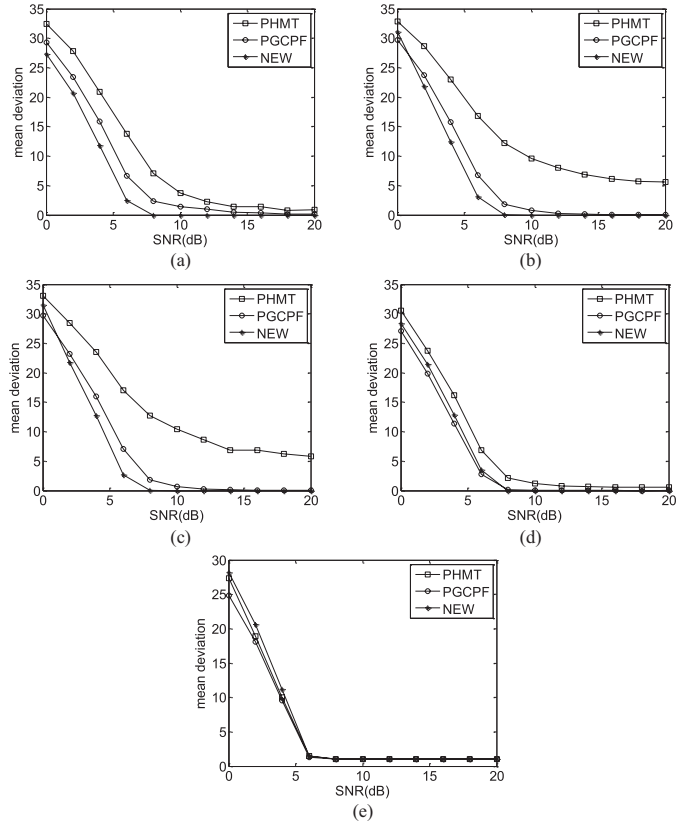


Fig. 12. Performance comparison of the three estimation methods in the case of noise. (a)–(e) Mean deviation of estimated component number versus the SNR in the 67th, 134th, 201th, 268th, and 335th range cell, respectively. (a) $K = 3$. (b) $K = 4$. (c) $K = 4$. (d) $K = 2$. (e) $K = 1$.

B. Real Data

The proposed algorithm has also been validated by processing real radar data of a ship target. The shore-based radar transmits LFM signals, the center frequency is 9.25 GHz, the bandwidth is 500 MHz, the pulse length is 600 μ s, the pulse repetition frequency is 200 Hz, the pulse number is 256, and the slant-range cell number is 256. The range between the radar and the target is 6 km. The ship with 24 m lengthwise is moving away from the LOS of the radar with a velocity of about 8 m/s.

The results relative to range compression and motion compensation are shown in Fig. 13. Then the parameter estimation of signal in each range cell can be carried out. The component numbers of the signal in several range cells obtained by applying different algorithms are listed in Table VIII. We notice that these algorithms have similar attributes in the cases shown in Tables VII and VIII. The results produced by the PHMT method have more components than obtained by the PGCPF method and the proposed method.

In order to quantitatively evaluate the performances of these imaging algorithms, we use the entropy of image data as a metric. The definition of entropy for $|I(m, n)|^2$ is [20]

$$E = \sum_m \sum_n \frac{|I(m, n)|^2}{S} \ln \frac{S}{|I(m, n)|^2}$$

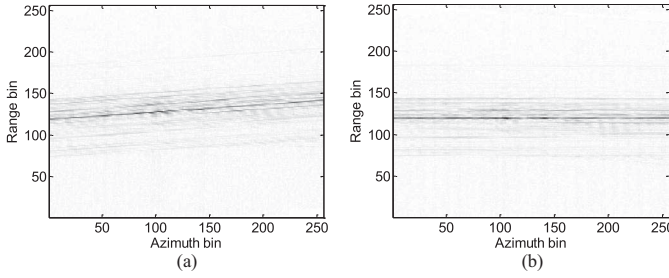


Fig. 13. Images after (a) range compression and (b) motion compensation.

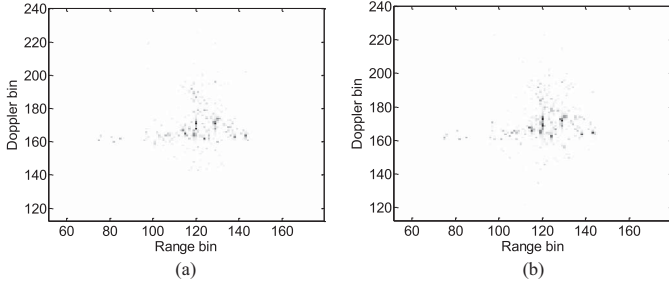


Fig. 14. Images via the PHMT-based algorithm at time (a) $t = 0.105$ s and (b) $t = 0.195$ s.

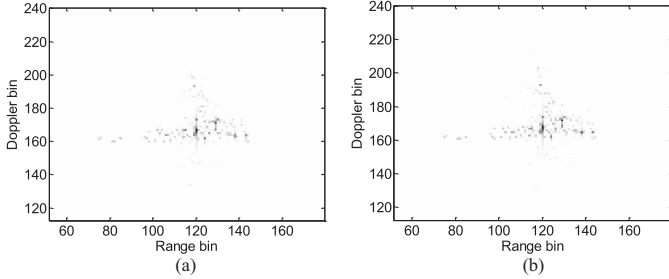


Fig. 15. Images via the PGCPF-based algorithm at time (a) $t = 0.105$ s and (b) $t = 0.195$ s.

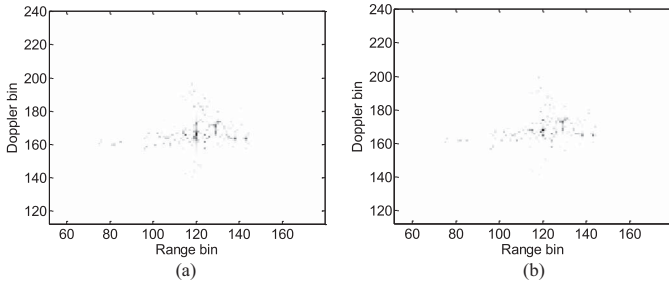


Fig. 16. Images via the proposed algorithm at time (a) $t = 0.105$ s and (b) $t = 0.195$ s.

where

$$S = \sum_m \sum_n |I(m, n)|^2.$$

In general, a smaller entropy implies better focused quality of image. The entropy of image data at different times is calculated and listed in Table IX. Figs. 14–16 show the corresponding images obtained by the PHMT-based, the PGCPF-based, and the proposed methods, respectively.

In Table IX, we can see that the entropies of image data produced by the PHMT algorithm are larger than those of

TABLE VIII
COMPONENT NUMBER IN SOME RANGE BINS

	115th Bin	120th Bin	129th Bin	138th Bin	143th Bin
PHMT	7	4	8	2	3
PGCPF	4	2	4	2	3
NEW	4	3	3	2	2

TABLE IX
ENTROPIES OF ISAR IMAGES

	$t = 0.105$ s	$t = 0.195$ s
PHMT	4.5185	4.7017
PGCPF	4.2510	4.2504
NEW	4.2386	3.8120

the other two, which implies that the PHMT algorithm has poor ability to reconstruct the image of the target. Too many scatterers exist in Fig. 14 when compared with Figs. 15 and 16. The entropy of image data produced by the PGCPF algorithm is comparable to that of the proposed algorithm, which implies that both of them can produce similar quality images. Additionally, the running times of the PHMT-based, the PGCPF-based, and the proposed methods are 44, 711, and 132 s, respectively. The PGCPF algorithm still suffers from a heavy computational burden. Therefore, the new algorithm has a much better overall performance than the other two algorithms, i.e., it not only produces good quality images but also can be carried out efficiently.

VI. CONCLUSION

In this paper, we studied parametric ISAR RID imaging of a ship target. After range compression and motion compensation, the echo signal in a range cell was modeled as a multicomponent QFM signal. Efficient and precise parameter estimation for the signal is a key point for a fast and accurate ISAR data processor. A new parameter estimation method for the QFM signal was presented. We have shown that the proposed method does not suffer from the considerable troublesome cross-term interference and heavy computational burden because of its moderate order of nonlinearity, effective coherent integration, and efficient CZT. Combined with the RID technique, a new imaging algorithm was illustrated and applied to reconstruct high-quality instantaneous ISAR images. The performance of the proposed ISAR imaging algorithm was validated by experimental results of simulated data and real data, which showed that the proposed algorithm serves as a good candidate for ISAR imaging of a ship target.

APPENDIX A

In this appendix, we discuss the criterion for the selection of the two zoom factors P_t and P_r in our proposed algorithm. Selecting a proper zoom factor can avoid spectrum aliasing and decrease estimation error as far as possible. For any PPS with order P , it will be assumed that

$$|a_p| \leq \frac{1}{2p \left(\frac{N}{2}\right)^{(p-1)} (\Delta t)^p}, \quad p = 1, 2, \dots, P. \quad (A1)$$

The reason for this restriction is to avoid ambiguities due to the periodicity of digital spectra. For a QFM signal, we have

$$|a_1| \leq \frac{1}{2\Delta t}, \quad |a_2| \leq \frac{1}{2N(\Delta t)^2} \quad \text{and} \quad |a_3| \leq \frac{2}{3N^2(\Delta t)^3}. \quad (\text{A2})$$

By using the proposed method, the third-order and second-order coefficients of the QFM signal can be estimated as

$$\hat{a}_3 = \frac{P_t}{6} \cdot \frac{1}{N\Delta t} \cdot k_0, \quad -\frac{N}{2} \leq k_0 < \frac{N}{2} \quad (\text{A3})$$

$$\hat{a}_2 = \frac{P_\tau}{2} \cdot \frac{1}{N\Delta t} \cdot l_0, \quad -\frac{N}{2} \leq l_0 < \frac{N}{2}. \quad (\text{A4})$$

Obviously, we have

$$\max\{|\hat{a}_3|\} = \max\left\{\left|\frac{P_t}{6\Delta t} \cdot \frac{k_0}{N}\right|\right\} = \frac{1}{2} \left|\frac{P_t}{6\Delta t}\right| \quad (\text{A5})$$

$$\max\{|\hat{a}_2|\} = \max\left\{\left|\frac{P_\tau}{2\Delta t} \cdot \frac{l_0}{N}\right|\right\} = \frac{1}{2} \left|\frac{P_\tau}{2\Delta t}\right|. \quad (\text{A6})$$

Let

$$\max\{|\hat{a}_3|\} \geq \frac{2}{3N^2(\Delta t)^3} \quad (\text{A7})$$

$$\max\{|\hat{a}_2|\} \geq \frac{1}{2N(\Delta t)^2}. \quad (\text{A8})$$

Hence under the limitation of

$$P_t \geq \frac{8}{N^2(\Delta t)^2} \quad (\text{A9})$$

$$P_\tau \geq \frac{2}{N(\Delta t)} \quad (\text{A10})$$

the spectrum aliasing can be avoided in the general assumed case. When the coefficients are smaller than the upper bound as shown in (A1), smaller zoom factors can be used to increase estimation accuracy. We suggest $P_t = 6/N^2(\Delta t)^2$ and $P_\tau = 2/N(\Delta t)$ empirically.

APPENDIX B

In this appendix, we show that the PGCPF algorithm will generate a wrong estimation when a signal contains the same quadratic phase coefficient components.

We assume that the signal, for the sake of simplicity, is

$$x(n) = x_1(n) + x_2(n) = e^{j\Phi_1(n)} + e^{j\Phi_2(n)} \quad (\text{B1})$$

where

$$\Phi_1(n) = a_{11}n + a_{12}n^2 + a_{13}n^3 \quad (\text{B2})$$

$$\Phi_2(n) = a_{21}n + a_{22}n^2 + a_{23}n^3. \quad (\text{B3})$$

The GCPF of signal $x(n)$ is

$$\text{GCPF}(n, k) = \sum_{m=0}^{(N-1)/2} y_x(n, m) e^{-jknm^2} \quad (\text{B4})$$

where $y_x(n, m) = x(n+m)x(n-m)x^*(-n+m)x^*(-n-m)$.

$y_x(n, m)$ can be expressed as

$$y_x(n, m) = y_{x_1, x_1}(n, m) + y_{x_2, x_2}(n, m) + y_{x_1, x_2}(n, m) + y_{x_2, x_1}(n, m) + \dots \quad (\text{B5})$$

where

$$y_{x_1, x_1}(n, m) = x_1(n+m)x_1(n-m) \cdot x_1^*(-n+m)x_1^*(-n-m) \quad (\text{B6})$$

$$y_{x_2, x_2}(n, m) = x_2(n+m)x_2(n-m) \cdot x_2^*(-n+m)x_2^*(-n-m) \quad (\text{B7})$$

$$y_{x_1, x_2}(n, m) = x_1(n+m)x_1(n-m) \cdot x_2^*(-n+m)x_2^*(-n-m) \quad (\text{B8})$$

$$y_{x_2, x_1}(n, m) = x_2(n+m)x_2(n-m) \cdot x_1^*(-n+m)x_1^*(-n-m). \quad (\text{B9})$$

$y_{x_1, x_1}(n, m)$ and $y_{x_2, x_2}(n, m)$ are auto-terms of $x_1(n)$ and $x_2(n)$, while $y_{x_1, x_2}(n, m)$ and $y_{x_2, x_1}(n, m)$ are their cross-terms.

We can expand the function Φ by a second-order Taylor series expansion

$$\Phi_i(n-m) = \Phi_i(n) - \Phi_i'(n)m + \frac{1}{2}\Phi_i''(n)m^2 \quad (\text{B10})$$

$$\Phi_i(n+m) = \Phi_i(n) + \Phi_i'(n)m + \frac{1}{2}\Phi_i''(n)m^2. \quad (\text{B11})$$

Then, the auto-term $y_{x_1, x_1}(n, m)$ can be rewritten as

$$\begin{aligned} y_{x_1, x_1}(n, m) &= x_1(n+m)x_1(n-m) \cdot x_1^*(-n+m)x_1^*(-n-m) \\ &= \exp\{j[2\Phi_1(n) + \Phi_1''(n)m^2]\} \\ &\quad \cdot \exp\{-j[2\Phi_1(-n) + \Phi_1''(-n)m^2]\} \\ &= \exp\{j[(2a_{12} + 6a_{13}n)m^2]\} \\ &\quad \cdot \exp\{-j[(2a_{12} - 6a_{13}n)m^2]\} \cdot \exp(j\phi_{11}) \\ &= \exp(j12a_{13}nm^2) \cdot \exp(j\phi_{11}) \end{aligned} \quad (\text{B12})$$

where $\phi_{11} = 2a_{11}n + 2a_{13}n^3$.

Similarly, the auto-term $y_{x_2, x_2}(n, m)$ is

$$y_{x_2, x_2}(n, m) = \exp(j12a_{23}nm^2) \cdot \exp(j\phi_{22}) \quad (\text{B13})$$

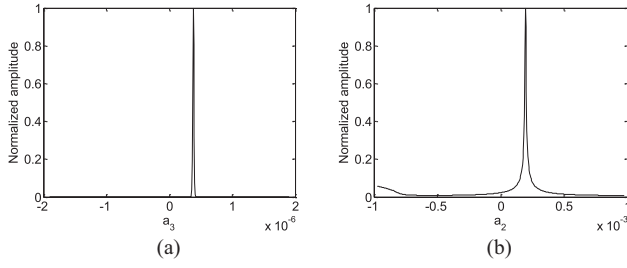
where $\phi_{22}(n) = 2a_{21}n + 2a_{23}n^3$.

For the cross-terms, $y_{x_1, x_2}(n, m)$ can be rewritten as

$$\begin{aligned} y_{x_1, x_2}(n, m) &= x_1(n+m)x_1(n-m) \cdot x_2^*(-n+m)x_2^*(-n-m) \\ &= \exp\{j[2\Phi_1(n) + \Phi_1''(n)m^2]\} \\ &\quad \cdot \exp\{-j[2\Phi_2(-n) + \Phi_2''(-n)m^2]\} \\ &= \exp\{j[(2a_{12} + 6a_{13}n)m^2]\} \\ &\quad \cdot \exp\{-j[(2a_{22} - 6a_{23}n)m^2]\} \cdot \exp(j\phi_{12}) \\ &= \exp[j(2a_{12} - 2a_{22})m] \\ &\quad \cdot \exp[j(6a_{13} + 6a_{23})nm^2] \cdot \exp(j\phi_{12}) \end{aligned} \quad (\text{B14})$$

where $\phi_{12} = (a_{11} + a_{21})n + (a_{12} - a_{22})n^2 + (a_{13} + a_{23})n^3$. Assume that the signal $x(n)$ contains the same quadratic phase coefficient components, i.e., $a_{12} = a_{22}$; then we can obtain

$$y_{x_1, x_2}(n, m) = \exp(j6a_{13}nm^3 + j6a_{23}nm^2) \cdot \exp(j\phi_{12}) \quad (\text{B15})$$

Fig. 17. Estimations of (a) a_3 and (b) a_2 using the PHMT algorithm.

where $\phi_{12} = (a_{11} + a_{21})n + (a_{13} + a_{23})n^3$.

Similarly, the auto-term $y_{x_2, x_1}(n, m)$ is

$$y_{x_2, x_1}(n, m) = \exp(j6a_{13}nm^3 + j6a_{23}nm^2) \cdot \exp(j\phi_{21}) \quad (B16)$$

where $\phi_{21} = (a_{11} + a_{21})n + (a_{13} + a_{23})n^3$.

Substituting (B12), (B13), (B15), and (B16) into (B5), we obtain

$$\begin{aligned} y_x(n, m) = & \exp(j12a_{13}nm^2) \cdot \exp(j\phi_{11}) \\ & + \exp(j12a_{23}nm^2) \cdot \exp(j\phi_{22}) \\ & + 2 \exp(j6a_{13}nm^2 + j6a_{23}nm^2) \cdot \exp(j\phi_{12}). \end{aligned} \quad (B17)$$

Thus, the GCPF of the signal $x(n)$ can be expressed as

$$\begin{aligned} \text{GCPF}(n, k) = & \exp(j\phi_{11}) \sum_{m=0}^{(N-1)/2} \exp(-j(k - 12a_{13})nm^2) \\ & + \exp(j\phi_{22}) \sum_{m=0}^{(N-1)/2} \\ & \cdot \exp(-j(k - 12a_{23})nm^2) \\ & + 2 \exp(j\phi_{12}) \sum_{m=0}^{(N-1)/2} \\ & \cdot \exp(-j(k - 6a_{13} - 6a_{23})nm^2). \end{aligned} \quad (B18)$$

The PGCPF method use the product form of the GCPF, which is defined as

$$\text{PGCPF}(k) = \prod_{l=1}^L \text{GCPF}(n_l, k). \quad (B19)$$

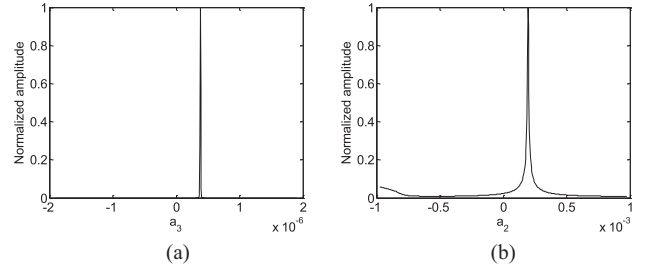
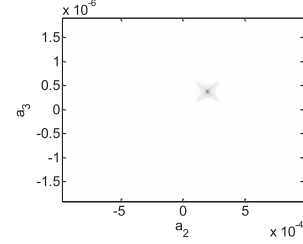
From (A18) and (B19), we can see that

$$\arg \max_k |\text{PGCPF}(n, k)| / 12 = \frac{a_{13} + a_{23}}{2}. \quad (B20)$$

Hence, the estimated result is

$$\hat{a}_{13} = \frac{a_{13} + a_{23}}{2}. \quad (B21)$$

Then PGCPF fails to estimate parameters of the signal in this case.

Fig. 18. Estimations of (a) a_3 and (b) a_2 using the PGCPF algorithm.Fig. 19. Estimations of a_3 and a_2 using the proposed algorithm.

APPENDIX C

In this appendix, the ranges of parameter estimation in the experiment shown in Section V are given. From the axes in Figs. 17–19 (in which the parameters of the testing signal are given in Table I), it can be ensured that the ranges of parameter estimation are the same for the three algorithms.

ACKNOWLEDGMENT

The authors would like to thank M. D. Xing and J. P. Sun for their valuable suggestions, J. Zhao for English language support, and the anonymous reviewers and the Associate Editor for their valuable help.

REFERENCES

- [1] D. L. Mensa, *High Resolution Radar Cross-Section Imaging*. Norwood, MA, USA: Artech House, 1991.
- [2] D. R. Wehner, *High Resolution Radar*. Norwood, MA, USA: Artech House, 1995.
- [3] F. Berizzi, E. D. Mese, M. Diani, and M. Martorella, "High-resolution ISAR imaging of maneuvering targets by means of the range instantaneous doppler technique: Modeling and performance analysis," *IEEE Trans. Imag. Process.*, vol. 10, no. 12, pp. 1880–1890, Dec. 2001.
- [4] M. Martorella, N. Acito, and F. Berizzi, "Statistical CLEAN technique for ISAR imaging," *IEEE Trans. Geosci. Remote Sens.*, vol. 45, no. 11, pp. 3552–3560, Nov. 2007.
- [5] Y. Li, R. Wu, M. Xing, and Z. Bao, "Inverse synthetic aperture radar imaging of ship target with complex motion," *IET Radar Sonar Navigat.*, vol. 2, no. 6, pp. 395–403, Dec. 2008.
- [6] M. Y. Abdul Gaffar, W. A. J. Nel, and M. R. Inggs, "Selecting suitable Coherent processing time window lengths for ground-based ISAR imaging of cooperative sea vessels," *IEEE Trans. Geosci. Remote Sens.*, vol. 47, no. 9, pp. 3231–3240, Sep. 2009.
- [7] Y. Wang and Y. Jiang, "ISAR imaging of a ship target using product high-order matched-phase transform," *IEEE Geosci. Remote Sens. Lett.*, vol. 6, no. 4, pp. 658–661, Oct. 2009.
- [8] Y. Wang and Y. Jiang, "ISAR imaging of maneuvering target based on the L-Class of fourth-order complex-lag PWVD," *IEEE Trans. Geosci. Remote Sens.*, vol. 48, no. 3, pp. 1518–1527, Mar. 2010.
- [9] J. M. Munoz-Ferreras and F. Perez-Martinez, "On the Doppler spreading effect for the Rang-Instantaneous-Doppler technique in inverse synthetic aperture radar imagery," *IEEE Geosci. Remote Sens. Lett.*, vol. 7, no. 1, pp. 180–184, Jan. 2010.
- [10] L. Zhang, Z. Qiao, M. Xing, Y. Li, and Z. Bao, "High-resolution ISAR imaging with sparse stepped-frequency waveforms," *IEEE Trans. Geosci. Remote Sens.*, vol. 49, no. 11, pp. 4630–4651, Nov. 2011.

- [11] V. C. Chen and S. Qian, "Joint time-frequency transform for Radar Range-Doppler imaging," *IEEE Trans. Aerosp. Electron. Syst.*, vol. 34, no. 2, pp. 486–499, Apr. 1998.
- [12] V. C. Chen and H. Ling, *Time-Frequency Transforms for Radar Imaging and Signal Analysis*. Norwood, MA, USA: Artech House, 2002.
- [13] X. G. Xia, G. Y. Wang, and V. C. Chen, "Quantitative SNR analysis for ISAR imaging using joint time-frequency analysis-short time fourier transform," *IEEE Trans. Aerosp. Electron. Syst.*, vol. 38, no. 2, pp. 649–659, Feb. 2002.
- [14] Y. Wu and D. C. Munson, "Wide-angle ISAR passive imaging using smoothed pseudo Wigner-Ville distribution," in *Proc. IEEE Radar Conf.*, May. 2001, pp. 363–368.
- [15] M. Xing, R. Wu, Y. Li, and Z. Bao, "New ISAR imaging algorithm based on modified Wigner-Ville distribution," *IET Radar Sonar Navigat.*, vol. 3, no. 1, pp. 70–80, Feb. 2009.
- [16] L. Zhang and D. S. Si, "A novel ISAR algorithm for the imaging of ship targets based on AM-LFM model," in *Proc. IEEE 10th Int. Conf. Signal Process.*, Oct. 2010, pp. 2147–2151.
- [17] Y. Wang and Y. Jiang, "Inverse synthetic aperture radar imaging of maneuvering target based on the product generalized cubic phase function," *IEEE Geosci. Remote Sens. Lett.*, vol. 8, no. 5, pp. 958–962, Sep. 2011.
- [18] L. R. Rabiner, R. W. Schafer, and C. M. Rader, "The chirp z-transform algorithm and its applications," *Bell Syst. Tech. J.*, vol. 48, pp. 1249–1292, May 1969.
- [19] A. V. Oppenheim and R. W. Schafer, *Discrete-Time Signal Processing*. London, U.K.: Prentice-Hall, 1989, pp. 623–628.
- [20] J. Wang, X. Liu, and Z. Zhou, "Minimum-entropy phase adjustment for ISAR," *IEEE Proc. Radar Sonar Navigat.*, vol.151, no. 4, pp. 203–209, Aug. 2004.



Xia Bai was born in Anshan, China, in 1978. She received the B.S. degree from the Changchun Institute of Posts and Telecommunications, Changchun, China, in 2000, and the Ph.D. degree from the Beijing University of Aeronautics and Astronautics, Beijing, China, in 2006.

She was a Post-Doctoral Researcher with the Beijing University of Aeronautics and Astronautics from 2006 to 2008. Since December 2008, she has been a Faculty Member with the Beijing Institute of Technology, Beijing, China. Her current research

interests include synthetic aperture radar (SAR) and inverse SAR signal processing, compressive sensing, time-frequency analysis, and remote sensing of the ocean using radar techniques.



Ran Tao (M'00–SM'04) was born in Nanjing, China, in 1964. He received the B.S. degree from the Hefei College of Electronic Engineering, Hefei, China, in 1985, and the M.S. and Ph.D. degrees from the Harbin Institute of Technology, Harbin, China, in 1990 and 1993, respectively.

He is currently a Professor with the School of Information and Electronics, Beijing Institute of Technology, Beijing, China. He has been a Distinguished Professor of Changjiang Scholars Program since 2009 and a Chief Professor of the Program for Changjiang Scholars and Innovative Research Team in University since 2010. His current research interests include fractional Fourier transform theory with applications for radar and communication systems.

Dr. Tao is currently the Vice Chair of IEEE China Council and the Chair of Technical Activity committee of IEEE Beijing Section. He is the Vice Chair of the International Union of Radio Science (URSI) China Council and a member of Wireless Communication and Signal Processing Commission of URSI. He was a recipient of National Science Foundation of China for Distinguished Young Scholars in 2006 and the Ministerial Science and Technology First-Grade Award in 2006 and 2007.



Zhijiao Wang was born in Shijiazhuang, China, in 1987. She received the B.S. degree from Yanshan University, Qinhuangdao, China, in 2009, and the M.S. degree from Beijing Institute of Technology, Beijing, China, in 2012.

Her current research interests include the field of synthetic aperture radar (SAR) and inverse SAR imaging.



Yue Wang was born in Danyang, China, in 1932. He received the B.S. degree in radar engineering from Xidian University, Shaanxi, China, in 1956.

He was the President of the Beijing Institute of Technology, Beijing, China, from 1993 to 1997. He is currently the President Emeritus of the Beijing Institute of Technology. His current research interests include information system theory and technology, and multiagent theory.

Prof. Wang is a Fellow of the Chinese Academy of Sciences and the Chinese Academy of Engineering.